Title
Evaluating the utility of multispectral information in delineating the areal extent of precipitation

Journal
Journal of Hydrometeorology, 10(3)

ISSN
1525-755X

Authors
Behrangi, A
Hsu, KL
Imam, B
et al.

Publication Date
2009-08-06

DOI
10.1175/2009JHM1077.1

Evaluating the Utility of Multispectral Information in Delineating the Areal Extent of Precipitation

ALI BEHRANGI, KUO-LIN HSU, BISHER IMAM, AND SOROOSH SOROOSHIAN

Center for Hydrometeorology and Remote Sensing (CHRS), The Henry Samueli School of Engineering, Department of Civil and Environmental Engineering, University of California, Irvine, Irvine, California

ROBERT J. KULIGOWSKI

NOAA/NESDIS/Center for Satellite Research and Applications (STAR), Camp Springs, Maryland

(Manuscript received 16 July 2008, in final form 6 January 2009)

ABSTRACT

Data from geosynchronous Earth-orbiting (GEO) satellites equipped with visible (VIS) and infrared (IR) scanners are commonly used in rain retrieval algorithms. These algorithms benefit from the high spatial and temporal resolution of GEO observations, either in stand-alone mode or in combination with higher-quality but less frequent microwave observations from low Earth-orbiting (LEO) satellites. In this paper, a neural network–based framework is presented to evaluate the utility of multispectral information in improving rain/no-rain (R/NR) detection. The algorithm uses the powerful classification features of the self-organizing feature map (SOFM), along with probability matching techniques to map single- or multispectral input space into R/NR maps. The framework was tested and validated using the 31 possible combinations of the five *Geostationary Operational Environmental Satellite 12* (*GOES-12*) channels. An algorithm training and validation study was conducted over the conterminous United States during June–August 2006. The results indicate that during daytime, the visible channel (0.65 μm) can yield significant improvements in R/NR detection capabilities, especially when combined with any of the other four *GOES-12* channels. Similarly, for nighttime detection the combination of two IR channels—particularly channels 3 (6.5 μm) and 4 (10.7 μm)—resulted in significant performance gain over any single IR channel. In both cases, however, using more than two channels resulted only in marginal improvements over two-channel combinations. Detailed examination of event-based images indicate that the proposed algorithm is capable of extracting information useful to screen no-rain pixels associated with cold, thin clouds and identifying rain areas under warm but rainy clouds. Both cases have been problematic areas for IR-only algorithms.

1. Introduction

Significant advances in rainfall estimation from satellite observations have been achieved in recent years. With improved observations, algorithms, and processing power, satellite-based precipitation estimates are moving toward increasingly finer spatial and temporal resolutions. Although this provides unprecedented opportunities for new hydrological and meteorological applications, it brings about an additional challenge of satisfying the demand for high accuracy at the scales relevant to such applications.

Both geosynchronous Earth-orbiting (GEO) satellites equipped with visible (VIS) and infrared (IR) scanners and low earth orbiting (LEO) satellites equipped with passive microwave (PMW) sensors provide observations that are commonly used for rainfall retrieval. PMW rain-retrieval algorithms (e.g., Kummerow et al. 1996; Weng et al. 2003; Zhao and Weng 2002) have the advantage of being more ''physically based,'' as they are sensitive to actual hydrometeor content rather than just to cloud-top properties like IR and VIS algorithms. However, LEO satellites have a low sampling frequency relative to GEO satellites, which is a significant problem for short-term, rapid-response hydrometeorological applications. Meanwhile, the significantly higher sampling

Corresponding author address: Ali Behrangi, The Henry Samueli School of Engineering, Dept. of Civil and Environmental Engineering, University of California, Irvine, E.4130, Engineering Gateway, Irvine, CA 92697-2175.
E-mail: abehrang@uci.edu

DOI: 10.1175/2009JHM1077.1

rate of GEO satellites, coupled with the higher spatial resolutions of IR and VIS instruments, offers the ability to capture the temporal variability of rainfall at scales relevant to many applications, albeit indirectly and through inferential algorithms. Recognition of the above described benefits and limitations has motivated the development of numerous combination/blending rain retrieval algorithms (Adler et al. 1993; Huffman et al. 2001, 2007; Joyce et al. 2004; Kidd et al. 2003; Kuligowski 2002; Kummerow and Giglio 1995; Levizzani et al. 1996; Miller et al. 2001; Sorooshian et al. 2000; Todd et al. 2001; Turk et al. 2000, 2003; Xu et al. 1999). In a majority of combined algorithms, precipitation rate is directly calculated from a GEO-based IR-only (~11 μm) image using PMW-derived relationships between GEO-based IR data and rain intensity. Therefore, GEO-based precipitation, whether standing alone or in combination with other sources, has broad effects and applications.

It is generally assumed that more intense precipitation is associated with colder cloud-top brightness temperature (Tb). However, the inverse relationship is not always true. High-altitude cirrus, for instance, is a very cold cloud and is often depicted as raining by IR-only algorithms, even though no rain actually occurs. Conversely, lower-level warm clouds (i.e., stratiform), which can be associated with precipitation, generally appear as nonraining clouds to IR-only algorithms. The misidentification of rain/no-rain (R/NR) areas is one of the major limitations of many IR-based techniques (Arkin and Xie 1994). It can reduce the effectiveness of long-term bias adjustment techniques (Tian et al. 2007).

In this paper, we explore the use of ''multispectral'' data as an alternative approach to improve GEO-based rain retrieval. As a first step, we select the binary problem of rainfall detection and develop a framework to test the utility of additional spectral channels. Our focus on the areal extent of precipitation leaves the estimation of rain rates to later work.

The scope of this paper is presented as follows: In section 2, we present a background on multispectral precipitation retrieval. Sections 3 and 4 introduce the proposed R/NR detection algorithm and its multispectral application, respectively. The validation of the algorithm is furnished in section 5, and two case studies are presented in section 6.

2. Background

Next to the thermal IR (~11 μm) channel, the VIS channel, which provides indirect measure of cloud thickness, is the second most commonly used band in GEO-based precipitation retrieval algorithms. Techniques that use both infrared and visible images to delineate rain and no-rain areas go back to the 1970s. Lovejoy and Austin (1979) developed a pattern matching technique that uses radar data to identify probabilities of R/NR occurrences in the normalized VIS–IR two-dimensional space and to delineate an optimal rain-area extent. Cheng et al. (1993) delineated precipitation areas using VIS–IR images for four distinct synoptic types: cold fronts, warm fronts, cold air convection, and mesoscale convective systems. They found that combined VIS and IR data perform better than using IR alone for all synoptic types. Subsequently, Cheng and Brown (1995) extended their analysis to refine the optimization of the aforementioned Lovejoy and Austin (1979) technique in a manner that accounts for synoptic patterns in rain-area delineation. Arguing that in midlatitudes the combination of VIS and IR imagery provides more rainfall-occurrence relevant information than IR only, Tsonis (1984) proposed a method that uses VIS–IR histograms to detect rain areas. Similarly, the IR and VIS combination has been extensively studied as input to rain-rate estimation techniques (Grassotti and Garand 1994; Griffith et al. 1978; Hsu et al. 1999; King et al. 1995; Negri and Adler 1987a,b; O'Sullivan et al. 1990). The effectiveness of other spectral bands in improving rain retrieval has also been investigated. Inoue (1987) showed that the brightness temperature difference (BTD) between 11 (Tb_{11}) and 12 μm (Tb_{12}) IR bands are useful in identifying cirrus clouds. Thin-cirrus pixels were found to coincide with $BTD_{(11\mu m,12\mu m)}$ values greater than 2.5 K. Kurino (1997) reported that image pixels where $BTD_{(11\mu m,12\mu m)}$ are greater than or equal to 3 K correspond to cirrus clouds with no rain, while areas whose $BTD_{(11\mu m,6.7\mu m)}$ are less than or equal to 0 K correspond to deep convective cloud with heavy rain. Using these three channels (11, 12, and 6.7 μm) along with composite digital radar data, he calculated three-dimensional (3D) lookup tables of probability of rain and mean rain rate to estimate both ''deep/shallow'' precipitation rates. Inoue and Aonashi (2000) used both the Visible Infrared Spectrometer (VIRS) and the precipitation radar (PR) on board the Tropical Rainfall Measuring Mission (TRMM) satellite to investigate the value of multispectral information. Selecting four parameters—the radiance ratio of 0.6 and 1.6 μm, $BTD_{(11\mu m,12\mu m)}$, $BTD_{(3.8\mu m,11\mu m)}$, and Tb_{11}—they suggested a number of thresholds for delineating rain areas and demonstrated the superiority of using multispectral information.

The utility of multispectral bands in capturing microphysical properties near cloud tops has also been the subject of many investigations. Pilewskie and Twomey (1987) showed that information relevant to cloud-top microphysics can be obtained from the reflected solar

radiation at several wavelengths in the near-infrared portion of the solar spectrum. Arking and Childs (1985) reported that the 3.7-μm band is very sensitive to the distribution of cloud drop sizes, thermodynamic phase, and particle shape. Rosenfeld and Gutman (1994) used Advanced Very High Resolution Radiometer (AVHRR) bands (0.65, 3.7, 10.8, and 12.0 μm) to analyze microphysical properties near the tops of potential rain clouds. Their findings indicate that the 3.7-μm band adds considerable information regarding precipitation processes in clouds, particularly those with top temperature greater than 245 K.

More recently, Ba and Gruber (2001) developed the Geostationary Operational Environmental Satellite (GOES) Multispectral Rainfall Algorithm (GMSRA). GMSRA uses five spectral bands—0.65, 3.9, 6.7, 11, and 12 μm—to estimate rainfall. The algorithm incorporates cloud-top Tb_{11} as a basis for estimation with concepts such as effective radii of cloud particles (Rosenfeld and Gutman 1994), spatial–temporal temperature gradients (Adler and Negri 1988; Vicente et al. 1998), and $BTD_{(11\mu m,6.7\mu m)}$, being employed to screen no-rain clouds. In a more recent study, Capacci and Conway (2005) investigated the benefits of multispectral images in delineating daytime precipitation areas during winter and in and around the United Kingdom. Using an artificial neural network (ANN), they tested 511 possible combinations of nine spectral bands (ranging from 0.6 to 12 μm) obtained from *Terra's* Moderate Resolution Imaging Spectroradiometer (MODIS) and the Spinning Enhanced Visible and Infrared Imager (SEVIRI) on board the Meteosat Second Generation (MSG) satellites. As a result, they reported remarkable improvement in skill by using multispectral data as opposed to use of only one visible or infrared channel.

Although in this study we focus on the five spectral bands within the *GOES-12* VIS–IR range, the proposed framework is inherently extensible. Our work differs from the analysis of Capacci and Conway (2005) in three aspects: First, we extend the analysis into a greater portion of the daylight hours by considering the effect of sun zenith angle (SZA) variation. Second, and more importantly, we employ the ANN-based self-organizing feature map (SOFM; Kohonen 1982) as opposed to the more traditional multilayer perceptual (MLP) neural networks. Third, we conduct our experiment over the contiguous United States as oppose to the United Kingdom. Therefore, different precipitation regimes are experienced, such as deep convective systems, which are not typical over the United Kingdom. As will be discussed later, by clustering input features into localized maps SOFM has the advantage of facilitating analysis capabilities, and by extension, of increasing the effectiveness of the method and the ability to interpret the nonlinear output resulting from ANN models. As described by Tapiador et al. (2004), ANNs are a viable alternative to physically based algorithms, especially where the underlying physical relationships between the studied quantities and/or processes are unclear. Readers interested in further discussion of the pros and cons of using neural networks in satellite precipitation estimation are referred to the above-mentioned work of Tapiador et al. (2004) and to the works of Hsu et al. (1997), among others.

3. R/NR detection algorithm

Figure 1 is a schematic overview of key steps pertaining to the development and validation of the proposed framework, as well as a visual depiction of the structure of the remainder of this manuscript. As seen in the figure (left side), the algorithm uses the SOFM to classify input features into clusters that are then used to assign R/NR designation to image pixels. In artificial neural networks' terminology, the term ''feature'' or ''input feature'' refers to any input that is introduced into the ANN. For example, the pixel's brightness temperature at a given wavelength (band) is called a feature, and the collection of features that are associated with each pixel is called a ''vector'' of features. Features associated with a given pixel can also be extracted from a window of neighboring pixels and may include the mean, standard deviation, range, and image texture indices (Wu et al. 1985). In this study, only the pixel value itself is used to facilitate more direct conclusions regarding the role of each spectral band or combination of them. We standardize each feature and then employ SOFM as a classifier to categorize input features into a number of clusters. Subsequently, R/NR probabilities are assigned to each cluster, based on radar observations. Following, and using the probability matching technique, a critical probability threshold (CPT) (Cheng. et al. 1993) is computed, which distinguishes clusters most likely associated with a rain event from those likely to represent no-rain situations. In the following sections, a more detailed description of the algorithms is provided.

a. Data preparation

Given a number of input features N, there are $2^N - 1$ possible ways of combining them. In our case the five *GOES-12* channels—VIS (Ch1; 0.65 μm), NIR (Ch2; 3.9 μm), water vapor (Ch3; 6.5 μm), and IR channels 4 (Ch4; 10.7 μm) and 6 (Ch6; 13.3 μm)—can be combined in 31 different ways. A number of issues must be considered when using all five channels of the *GOES-12*

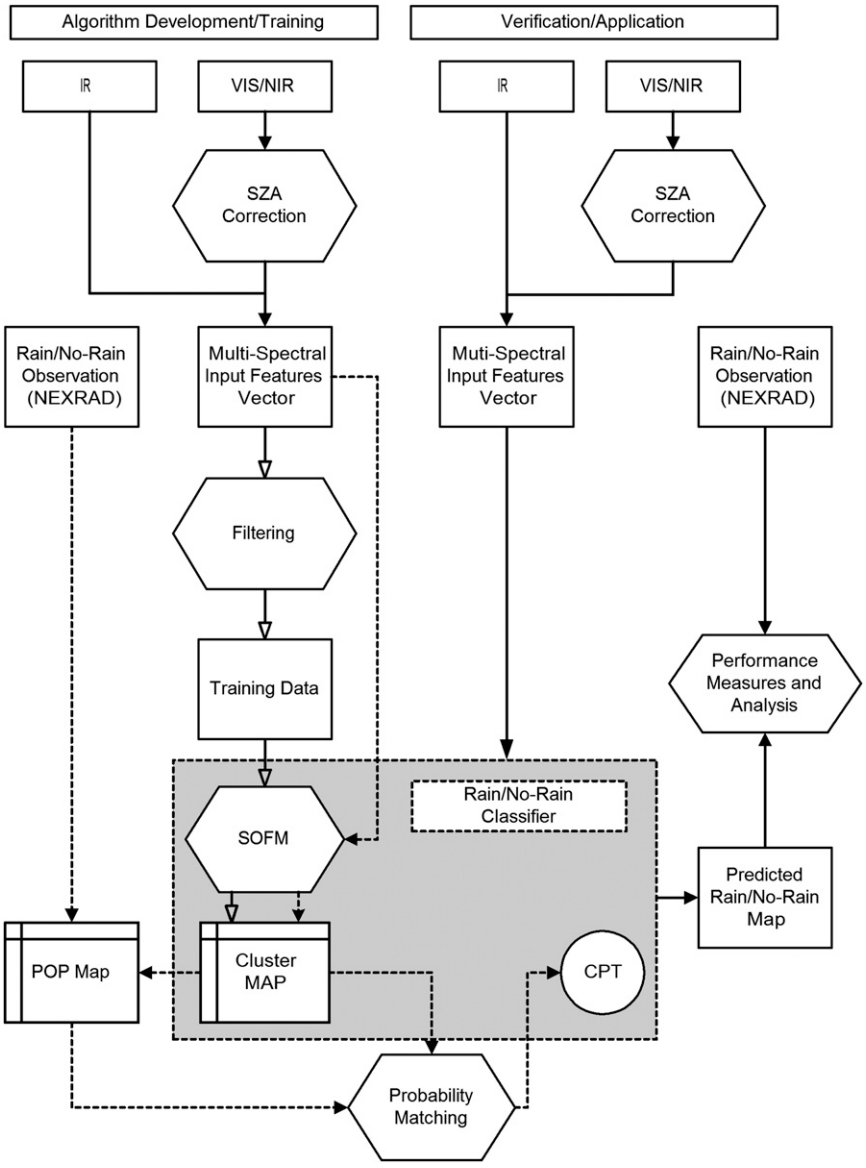

FIG. 1. Schematic overview of algorithm development and verification. Dotted arrows indicate supervised classification connections and unfilled arrows represent unsupervised classification connections. The trained SOFM, along with its cluster map and the critical probability threshold, represent the R/NR classifier (gray area). Notice that the procedures described in this figure are repeated for each of the 31 combinations.

satellite. First, Ch1 (0.65 μm) is only available during the daytime. Second, the reflection from both Ch1 and Ch2 (which has a reflection as well as an emission component) must be normalized to account for the effect of SZA variation. The mixed emitted and reflected radiation at Ch2 must be separated before adjusting the reflection component. Herein, this was performed using the thermal channel (Ch4) through Planck's radiation law (Rosenfeld and Gutman 1994). In addition, since the radiance at 3.9 μm is quite low (roughly three orders of magnitude lower than the radiance at 10.7 μm for a brightness temperature of 210 K), the precision of GOES brightness temperatures below 230 K is very poor, and ''saturation'' values below 200 K cannot be measured.

Two popular albedo normalization methods were investigated to select the more effective approach for SZA normalization. The first approach multiplies an observed albedo by its associated $(\cos\mathrm{SZA})^{-1}$, as in (Cheng et al. 1993; King et al. 1995), and the second approach uses the

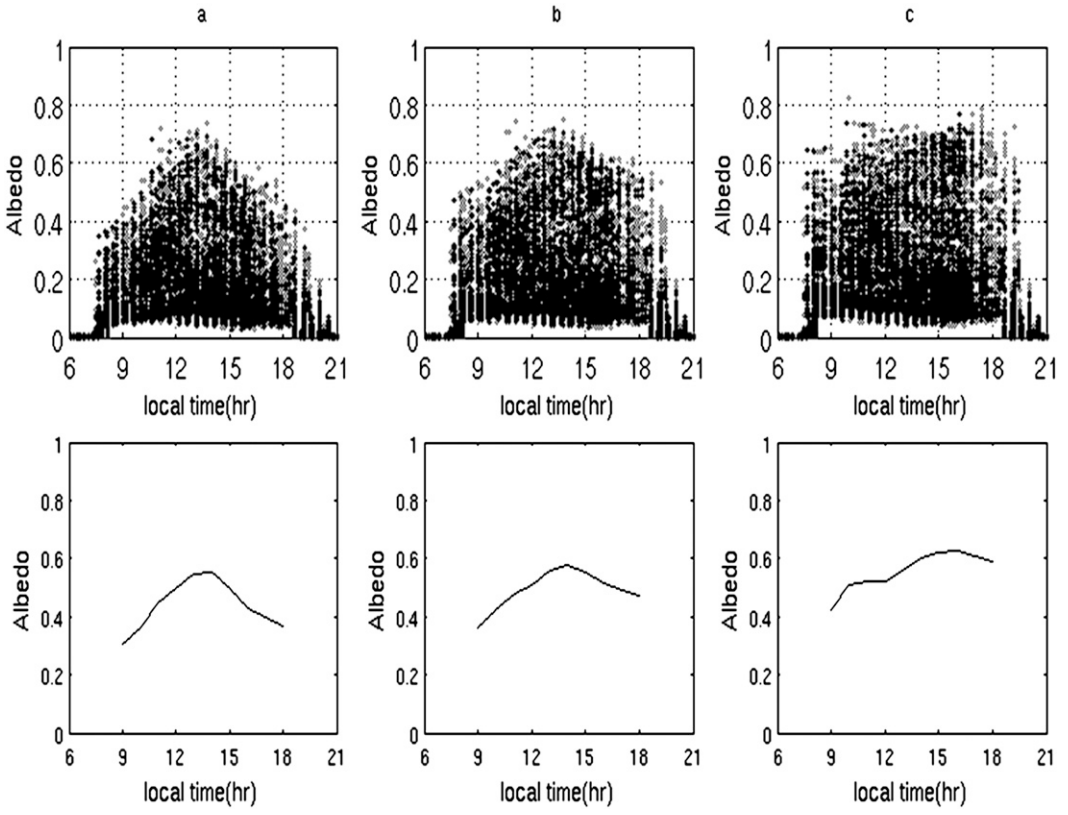

FIG. 2. Comparison of two albedo normalization methods for SZA diurnal variation. Albedo data obtained from *GOES-12* during Jun–Aug 2006, (a) without any normalization, (b) using $(\cos\mathrm{SZA})^{-1/2}$, and (c) using $(\cos\mathrm{SZA})^{-1}$. (top row) All pixels considered in the analysis with SZA $< 60°$. (bottom row) The 90th percentile of albedo associated with the SZA $< 60°$.

inverse square root of cosine: $(\cos\mathrm{SZA})^{-1/2}$ (Minnis and Harrison 1984; Tsonis and Isaac 1985). Figure 2 shows a comparison of the two methods when applied to a large sample of pixels that represents regional variability of local time SZA over the contiguous United States during summer. As mentioned by King et al. (1995), SZA correction is deemed effective when the normalized albedo shows little diurnal variation at high albedo values, associated with very bright clouds. As seen in the Fig. 2c, normalizing by $(\cos\mathrm{SZA})^{-1}$ seems to be more effective than by $(\cos\mathrm{SZA})^{-1/2}$ (Fig. 2b) when compared to unnormalized values (Fig. 2a). Because of uncertainties associated with SZA greater than 60° (early morning and late evening hours), normalization was only applied within SZA $< 60°$. On the basis of the overall results, we conclude that $\cos^{-1}(\mathrm{SZA})$ is reasonable to normalize albedo and the reflected component of Ch2 when SZA $< 60°$. Note that the simple method employed here assumes that the reflected radiation field is isotropic and thus much more subject to error than a more rigorous approach of directly retrieving the cloud microphysical properties from reflected solar radiation, such as that presented in Nakajima and King (1990) and Nakajima et al. (1991). However, since the purpose of this paper is to demonstrate the potential utility of these bands for R/NR discrimination, this approximation should be sufficient for this study.

The remaining channels (3, 4, and 6) are less sensitive to diurnal effects and do not require adjustment. Although the latter three channels can be used during daytime and nighttime, the study is restricted to only daytime images (with SZA $< 60°$) to ensure the homogeneity of the images used in the proceeding comparisons. Arguably, any conclusion made regarding the seven possible combinations of channels 3, 4, and 6 can be extrapolated to infer their potential use in detecting areal extent of precipitation during nighttime as well.

b. SOFM unsupervised training

The second stage of the proposed framework involves using a SOFM (Kohonen 1982) technique to classify input features into a number of groups called clusters. Training the SOFM occurs in the unsupervised mode

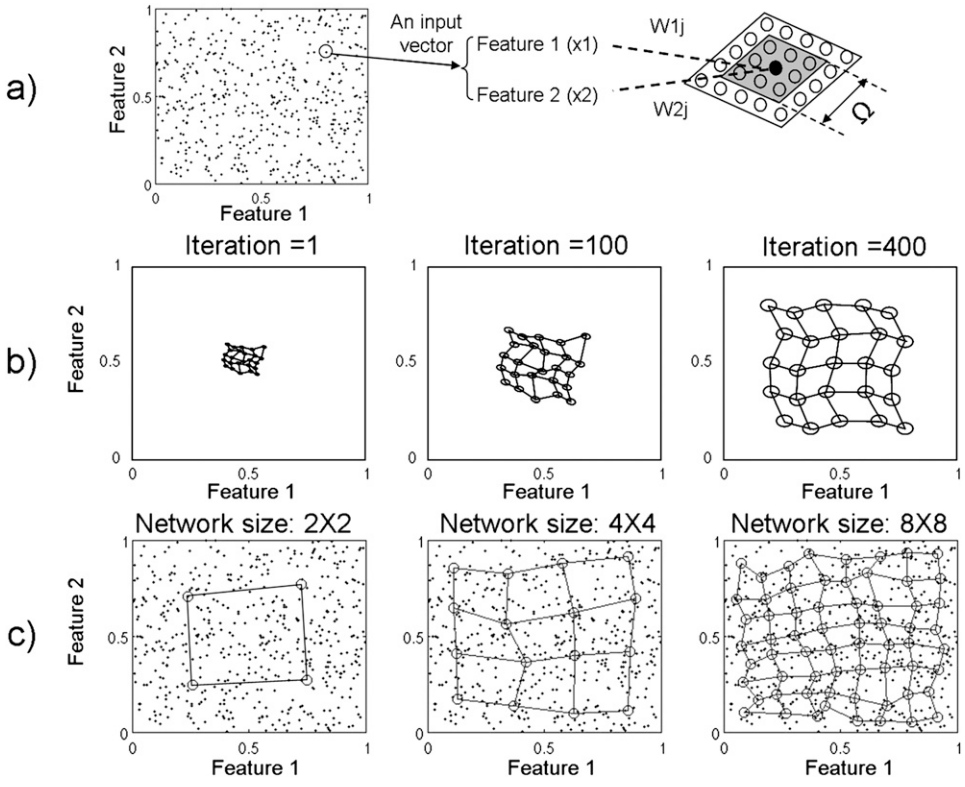

FIG. 3. A brief overview of the SOFM technique. (a) Presentation of a 2D input feature space into a 2D SOFM structure. (b) Expansion of the cluster centers during the recursive training process. (c) Representation of input space with respect to the number of cluster centers.

without introducing R/NR observations into the process. The unsupervised training improves the SOFM classification by reducing the noisiness that may result from uncertainties in precipitation measurement fields. Below is a brief description of the procedure; a detailed description is available in Hsu et al. (1999).

The SOFM divides the multidimensional feature space into a predetermined number of clusters arranged in a 2D structure. Theoretically, SOFM clusters can be arranged in any number of dimensions. However, as seen in section 3d, the 2D architecture of the SOFM clusters facilitates the visualization of the clusters, which is a valuable tool for interpreting the results. To describe the SOFM training process, an example using a two-dimensional feature map is demonstrated in Fig. 3. The process of the SOFM training consists of following steps:

Step I: Initialization. The cluster centers (weight vectors) are generated randomly near the center of standardized (between zero and one) input feature space (Fig. 3b, left panel).

Step II: Competition. The input feature vectors are presented one by one from the training dataset to the network and a distance d between each standardized input feature (x_i, $i = 1, \ldots n_0$) and the corresponding SOFM cluster center is calculated as

$$d_j = \left[\sum_{i=1}^{n_0} (x_i - w_{ij})^2\right]^{1/2}, \quad j = 1, \ldots, n_1 \qquad (1)$$

where, w_{ij} is the weight vector (connection parameter) of the SOFM from input feature i to the specified node j. For each input vector, the best matching SOFM cluster, c (winning cluster), is defined as the cluster that possesses the shortest distance d between the input feature vector and the SOFM connection weight vector w_{ij}, as follows:

$$d_c = \min(d_j), \quad \text{where} \quad j = 1, \ldots, n_1. \qquad (2)$$

Step III: Weight (cluster center) update. The wining cluster and its neighboring cluster centers (clusters within the gray area, with size Ω shown in Fig. 3a, right side) are moved toward the presented input vector with an already-defined learning rate η. Both

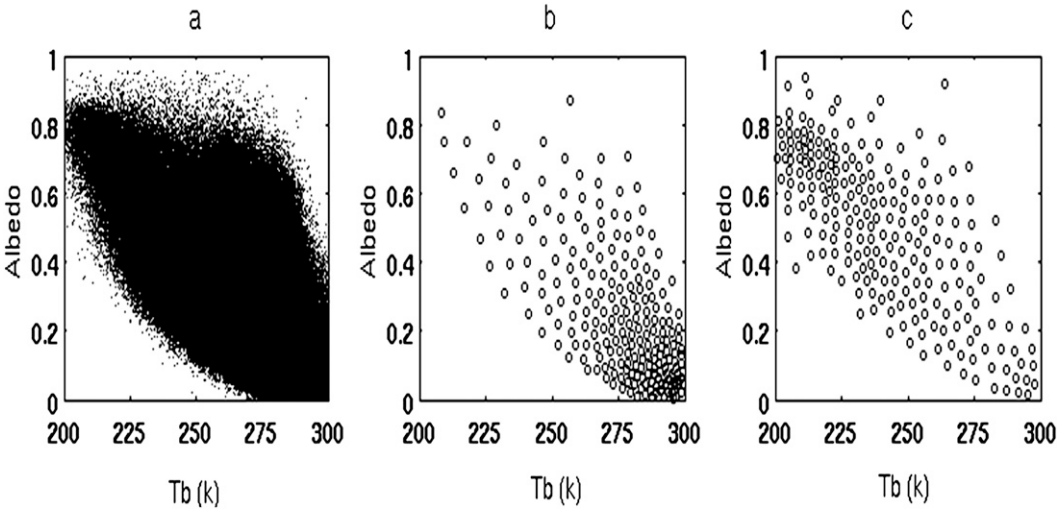

FIG. 4. Illustration of the role of filtering process to improve the representation of more likely rain situations. (a) Dataset used for the training the network. (b) Clusters arrangement before filtering. (c) Clusters arrangement after filtering. Notice the resulting shift in the concentration of clusters between the two cases.

η and Ω are reduced throughout the learning process, as described in Hsu et al. (1999).

Step IV: Recursive computation. Through a recursive process of competitive cluster selection and weight adjustment, cluster centers continue to evolve (see Fig. 3b) and finally become stable with respect to the decrease of learning rate and the neighborhood size.

After training, the trained SOFM has the ability to assign any arbitrary input feature vector $\mathbf{x}_i$ to the closest SOFM cluster center. As shown in Fig. 3c, increasing the number of trained clusters results in more detailed representation of the input feature space. A 2×2 cluster network (Fig. 3c, left panel) offers only four clusters, which poorly represent the input feature space, while a 8×8 network (Fig. 3c, right panel) includes 64 clusters, resulting in substantial improvement in representing input space details. Figure 3c also illustrates that clusters arranged into a two-dimensional discrete map preserves the topological order of feature vectors. This means that the 2D SOFM structure that we assigned before (Fig. 3a, left side) is projected into the input feature space and preserves the neighborhood connection of SOFM clusters (see Fig. 3c).

c. Filtering

In reality, the automatic clustering of input features may result in an undesirable representation of the system. Consider, for example, a 15×15 cluster network with a 2D input feature vector that includes albedo and $Tb_{10.7}$. By training the SOFM with a fully randomly sampled dataset (Fig. 4a), most of the clusters appear to be concentrated over the region of high brightness temperature and low albedo, representing clear-sky grid boxes (Fig. 4b). This, unfortunately, causes most of the SOFM clusters to explain those situations with little or no precipitation. To better represent cloudy areas with a higher possibility of precipitation occurrence, a sufficient number of clusters in the region of low Tb is required. Filtering the sample data ahead of the SOFM classification is one way to ameliorate this problem. Therefore, in the present study, a two-step filtering procedure is used. In the first step, all data samples are binned into a number of groups (here, 10 groups with unequal range), based on Ch4 brightness temperature. Then, the number of samples in the coldest bin is applied as an upper limit to screen data in the other bins: data from the warmer bins are randomly removed until the total count of data vectors in each bin matches the number of samples in the coldest temperature group. The redistribution results in a more desirable distribution of clusters in the input feature space and thus improves the representation of cloudy areas by the cluster centers (Fig. 4c).

d. Probability of precipitation for each cluster

At the end of the training step, the location of cluster centers in the input feature space (SOFM weights) is fixed. Afterward, the entire algorithm development dataset is processed through the SOFM network, and each input vector is assigned to the corresponding cluster in the SOFM layer. As described in section 4a, for each input vector (from satellite grid boxes), approximately coincident rain rate information is assigned from rain

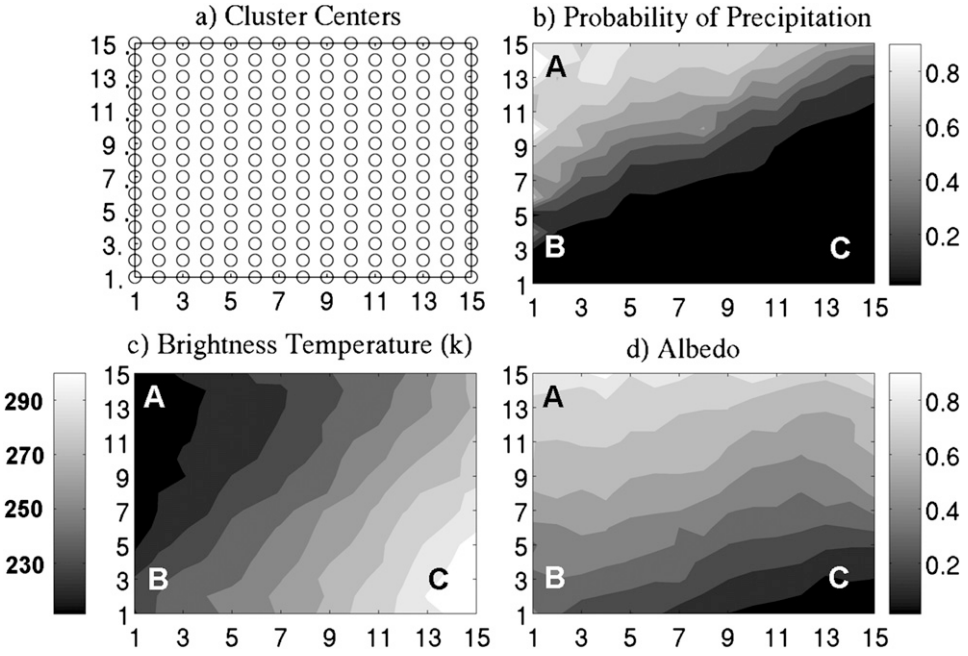

FIG. 5. Two-dimensional representation of clusters' arrangement and their corresponding maps of computed POP, albedo (Ch1), and brightness temperature (Ch4).

''observation.'' The next step is using rain ($\geq$0.1 mm h^{-1}) and no-rain ($<$0.1 mm h^{-1}) observations to compute a POP for each cluster (k) as

$$\mathrm{POP}_k = \frac{R_k}{(R_k + D_k)} \times 100, \quad k = 1, \ldots, n_1 \qquad (3)$$

where R_k and D_k are the total counts of rain and no-rain observations for each cluster, respectively.

As mentioned earlier, the SOFM clusters are arranged into a two-dimensional discrete map that preserves topological order. A two feature (Ch1 + Ch4) example is shown in Fig. 5 to describe how clusters (Fig. 5a) integrate input features into a two-dimensional map of POP (Fig. 5b). Visual inspection of Fig. 5 shows that high POP is mostly associated with low brightness temperature (Fig. 5c) and high albedo (Fig. 5d), which corresponds to cold and thick clouds (zone A). Also, cold, thin clouds (i.e., cirrus), generally characterized by low temperature and low albedo, correspond with lower POP (zone B). Naturally, clear sky during summertime corresponds with high brightness temperature, low albedo, and, as clearly shown, with low POP (zone C). In general, the accuracy of the above-defined POP depends on several factors, including the effectiveness of input features mapping, the issue of coregistration of satellite and radar observations, and the uncertainty in ground observation (i.e., radar) of R/NR pixels.

e. Critical probability threshold

Because R/NR delineation is a binary problem, a mechanism to separate R/NR clusters is needed. If we treat POP as an index of the likelihood of a rain or no-rain event, a critical probability threshold can then be defined to divide SOFM–POP cluster maps into SOFM-rain and no-rain clusters. To identify such a threshold, we use pattern matching techniques in manners similar to Lovejoy and Austin (1979) and Cheng et al. (1993). As implemented in this study, the pattern matching technique consists of the following steps. First, SOFM clusters are sorted in order of decreasing POP. Second, starting from the cluster with the highest POP, the total number of rain counts (obtained from all clusters) is reallocated to the top ranking clusters, one by one, up to their original (rain and no rain) counts. The reallocation continues until the total rain count is exhausted. The POP of the cluster at which this occurs is defined as the critical probability threshold (CPT). In essence, all the clusters with POP higher than CPT will be considered as rain with effective POP = 1 and those with lower values as no rain with effective POP = 0.

Identifying CPT marks the conclusion of the model's development phase. Indeed, the reduction of the dimensionality of the input features vector into a 2D SOFM map of clusters and the subsequent determination of POP and CPT is a robust feature that enhances our algorithm's extensibility to cope with a large

number of input channels and, consequently, computational cost. For each spectral combination, the trained SOFM and its cluster map along with CPT form the R/NR classifier (gray box in Fig. 1)

4. Algorithm application

a. Data

Three months (June, July and August 2006) of half-hourly *GOES-12* images with 0.04° × 0.04° spatial resolution were collected from the National Oceanic and Atmospheric Administration/National Environmental Satellite, Data, and Information Service (NOAA/NESDIS) Environmental Satellite Processing Center (ESPC) over the conterminous United States. In addition, hourly accumulated 4-km gridded radar rain rate estimates were obtained from the National Centers for Environmental Prediction (NCEP) Environmental Modeling Center (EMC) (Lin and Mitchell 2005) and remapped to a 0.04° latitude/longitude.

The dataset was divided into model development (calibration) subset and model validation/verification subset using a simple odd–even Julian day criterion. Images obtained on odd days were selected for training and model development, while even days were retained for model validation. A mask representing the effective beam height of 3 km (Maddox et al. 2002) was applied to screen radar rainfall observations that may not be reliable. Note that the hourly rainfall rate observation, described above, was assumed to be uniformly distributed within each hour (i.e., that the rain rate was constant with time) to allow the comparison with half-hourly GOES data. As for each *GOES-12* image, as described earlier, only pixels satisfying the SZA $< 60°$ at the time of image acquisition were introduced into the network.

b. SOFM size

As mentioned previously, the development of a SOFM network requires a predetermined number of clusters. In principle, a larger number of input features are better classified by a network with a larger number of clusters. However, a larger number of clusters can also substantially increase the computational demands of both network development and application. An optimal configuration, for our purposes, would be the one that ensures the stability of the model performance for the larger channel combination. Using a representative subset of the model development data, a sensitivity analysis of the model's performance, as measured by the equitable threat score (ETS; see next section), was conducted. The results of the sensitivity analysis for selected combinations are shown in Fig. 6. As seen from the figure, a 10 × 10 SOFM network is relatively sufficient to classify both small and large channel combinations. However, a 15 × 15 cluster network was selected as a proper SOFM size and implemented to each of the 31 possible combinations of spectral bands.

c. Performance measures

The equitable threat score is one of several verification statistics that can be computed from the binary-based contingency table. The table classifies the prediction outcome into the following four possibilities based on observation of R/NR occurrences:

- hits (H): number of pixels correctly classified as precipitation,
- misses (M): number of pixels incorrectly classified as no precipitation,
- false alarms (F): number of pixels incorrectly classified as precipitation,
- correct negatives (Z): number of pixels correctly classified as no precipitation.

A perfect prediction system would produce only hits and correct negatives and no misses or false alarms. But in reality, predictions produce both of the latter. The model's skill can then be described in terms of ratios of hits and/or misses to the observations. Among the most commonly used statistics are

- probability of detection: $$\mathrm{POD} = \frac{H}{H + M} \tag{4}$$
- false alarm ratio: $$\mathrm{FAR} = \frac{F}{H + F} \tag{5}$$
- bias estimate: $$\mathrm{BIAS} = \frac{H + F}{H + M} \tag{6}$$

POD and FAR range from 0 to 1, with perfection represented by a POD of 1 together with a FAR of 0. POD is sensitive to the number of hits, but it ignores false alarms; FAR, on the other hand, is sensitive to false alarms, but it ignores misses. As a result, a low POD can be increased by increasing the predicted rain coverage but such improvement would be at the cost of increasing false alarms. In general, BIAS considers both predictions and observations. A value of 1 indicates that predictions and observations have identical area coverage independent of location. As such, a perfect BIAS score does not necessarily indicate a perfect match of R/NR pixels between observed and predicted fields. Originally defined in (Gilbert 1884), the ETS, also called the Gilbert skill score (Schaefer 1990), is a modification of the commonly used threat score, also

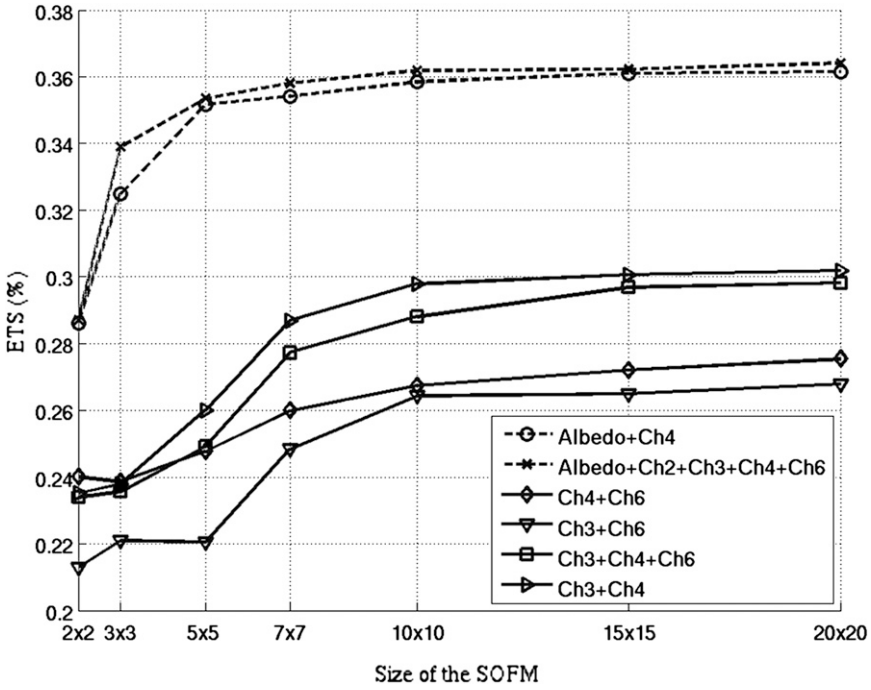

FIG. 6. Sensitivity of SOFM R/NR detection performance to number of clusters in the network for selected combinations.

known as the critical success index. ETS is computed as follows:

$$\mathrm{ETS} = \frac{H - C}{(H + F + M) - C}, \tag{7}$$

where

$$C = \frac{(H + M)(H + F)}{(H + F + M + Z)}.$$

Schaefer (1990) referred to C as the ''number of fortuitously correct forecasts'' or the number of hits that occur by chance. He argued that, among many possible skill scores, ETS is less sensitive to ''no forecast'' (Z) and is more accurate across both rare and more frequent events. Arguably, by subtracting fortuitously correct forecasts from the number of hits, and from the total number of threats ($H + M + F$), ETS becomes a more ''equitable'' score. ETS is commonly used in the verification of numerical weather prediction models and more specifically in verifying models' ability to capture rare extreme events (Stephenson 2003). The lower bound of ETS is $-1/3$, and it indicates that the model's skills are worse than the skill of a random prediction. A value of 0 would indicate that all the correct predictions may be attributed to chance, and a value of 1 indicates full correspondence between predicted and observed occurrences of the event being verified. In this study, ETS is used as the main skill score to cross compare the performances of the 31 spectral combinations during model validation. Other scores, such as POD, FAR, and BIAS, are computed but not shown here. These measures will be used to provide insight into specific case study events.

5. Results and verification

By considering the computational cost and goodness of the classification, about 56 000 filtered input vectors (out of approximately 6 000 000 input vectors) were used for SOFM classifications of each combination scenario. The clusters POP for each combination scenario was calculated using about 11 000 000 satellite–radar matched grid boxes, which were extracted from the calibration and training datasets. Finally, the CPT of each combination scenario was calculated and used to delineate rain area.

Table 1 summarizes the model validation results for all 31 channel combinations grouped by the number of channels in each combination in ascending order. Within each group, the combinations are listed in descending order of performance skill as measured by ETS. In addition to ETS, a performance gain/loss measure was computed as the ratio of gain/loss in performance compared to the performance measure associated with using Ch4 alone:

TABLE 1. Summary of validation results over the contiguous United States (Jun–Aug 2006).

Number of channels	Scenarios	ETS	Performance gain (%)	Rank	Effective period
One	Albedo	0.327	34.95	16	Day
	Ch2	0.261	7.78	28	Day
	Ch4	0.242	0	29	Day + night
	Ch6	0.226	−6.54	30	Day + night
	Ch3	0.209	−13.71	31	Day + night
Two	Albedo + Ch2	0.370	52.68	8	Day
	Albedo + Ch4	0.361	48.87	13	Day
	Albedo + Ch6	0.350	44.47	14	Day
	Albedo + Ch3	0.350	44.27	15	Day
	Ch2 + Ch3	0.294	21.20	20	Day
	Ch3 + Ch4	0.293	20.84	21	Day + night
	Ch2 + Ch6	0.284	17.15	24	Day
	Ch2 + Ch4	0.281	16.11	25	Day
	Ch4 + Ch6	0.273	12.58	26	Day + night
	Ch3 + Ch6	0.267	10.15	27	Day + night
Three	Albedo + Ch2 + Ch3	0.372	53.37	3	Day
	Albedo + Ch2 + Ch6	0.370	52.76	4	Day
	Albedo + Ch2 + Ch4	0.370	52.54	6	Day
	Albedo + Ch3 + Ch4	0.362	49.34	10	Day
	Albedo + Ch4 + Ch6	0.362	49.20	11	Day
	Albedo + Ch3 + Ch6	0.360	48.63	12	Day
	Ch2 + Ch3 + Ch4	0.295	21.62	18	Day
	Ch3 + Ch4 + Ch6	0.294	21.39	19	Day + night
	Ch2 + Ch3 + Ch6	0.290	19.87	22	Day
	Ch2 + Ch4 + Ch6	0.285	17.57	23	Day
Four	Albedo + Ch2 + Ch3 + Ch6	0.372	53.56	2	Day
	Albedo + Ch2 + Ch4 + Ch6	0.372	53.48	5	Day
	Albedo + Ch2 + Ch3 + Ch4	0.371	53.25	7	Day
	Albedo + Ch3 + Ch4 + Ch6	0.371	53.12	9	Day
	Ch2 + Ch3 + Ch4 + Ch6	0.295	21.63	17	Day
Five	Albedo + Ch2 + Ch3 + Ch4 + Ch6	0.372	53.59	1	Day

$$\%\ \text{Gain}_i = \frac{\text{ETS}_i - \text{ETS}_{\text{ch4}}}{\text{ETS}_{\text{ch4}}} \times 100, \qquad (8)$$

where i is the combination index. Channel 4 was chosen as the reference channel because it is the most commonly used band in IR-only rain retrieval algorithms.

From Table 1, it is clear that in comparison with other single channels, the visible channel (albedo) alone, with ETS (0.327) and ETS gain (34.95%), is very effective in delineating the areal extent of rain during the daytime. This is consistent with the partial results shown previously in Fig. 5 that demonstrate the value of albedo as an indirect measurement of cloud optical thickness in discerning the probability of precipitation. Combining albedo with any other channel, particularly with Ch2 (albedo + Ch2, ETS = 0.370) or Ch4 (albedo + Ch4, ETS = 0.361), scored better than albedo alone and much better than any combination of IR channels; however, increasing the number of channels beyond two yields marginal improvements. The marked improvement achieved by using visible data is consistent with previous studies (Capacci and Conway 2005; Cheng et al. 1993; Lovejoy and Austin 1979; Tsonis 1988).

The results in Table 1 also highlight the importance of Ch2 as the second-best channel during daytime in single-channel mode. The reflection component of Ch2 is a factor for the improved performance. The good performance of Ch2 (3.9 μm) is also consistent with Arking and Childs' (1985) findings that the relatively similar 3.7-μm channel is sensitive to cloud drop size distribution, thermodynamic phase, and particle shape. Our results also support the findings of several other studies that have argued in support of using the 3.7-μm channel, particularly during daytime (Rosenfeld and Gutman 1994; Rosenfeld and Lensky 1998).

An interesting observation from Table 1 is the strong complimentary role of the water vapor channel (Ch3), especially in conjunction with Ch4. In single-channel mode, Ch3 has a very low skill in discriminating raining from nonraining pixels. However, when used in combination with Ch4, significant improvement in skill (ETS) is obtained. This is partially consistent with the findings of previous authors (e.g., Ackerman 1996; Martin et al. 2008; Tjemkes et al. 1997), who argued that areas where Ch3 was warmer than Ch4 were regions where overshooting

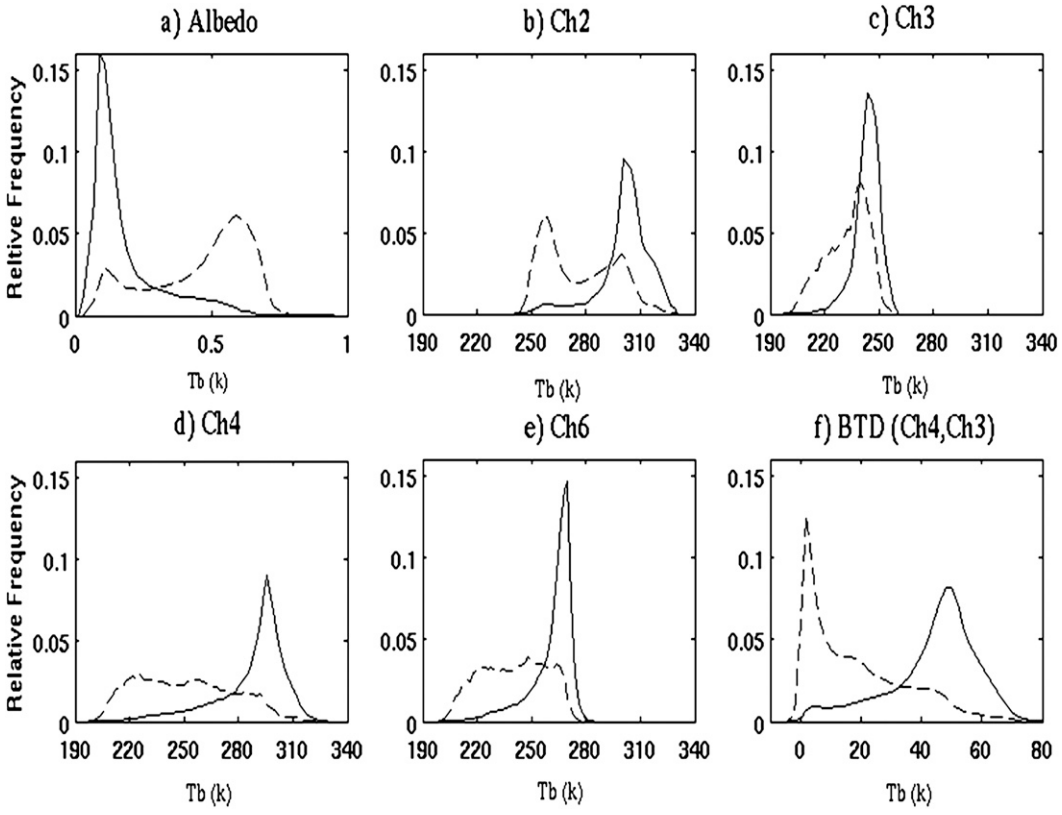

FIG. 7. (a) Relative frequency distributions of albedo, (b)–(e) Tb, and (f) BTD under rain (dashed line) and no-rain (solid line) conditions.

convective tops had ejected water vapor into the stratosphere, producing a warm water–vapor signal above cloud top. Although the performance of other combinations that include channel 3 along with albedo are better than the two-channel (Ch3 + Ch4) combination, the latter bears significant impacts for nighttime rain detection. At nighttime, the visible channel is not available, and Ch2 does not have the important reflection component. With both Ch3 and Ch4 being commonly available on most of the operational and research GEO satellites, the gain in nighttime rain detection performance through their combination is rather welcomed.

Further insight into the reason for the superior performance of the Ch3 + Ch4 combination in contrast with their individual contributions can be gained by comparing the distribution of their brightness temperature under rain and no-rain situations. Figure 7 shows the relative frequency distribution of single channels along with the BTD (Ch4, Ch3). The latter, to some extent, can reflect the combined effect of the two channels, and several studies (i.e., Inoue and Aonashi 2000; Kurino 1997; Lensky and Rosenfeld 2003; Schmetz et al. 1997) have already reported the utility of BTD (Ch4, Ch3) as an input to rain retrievals algorithm. For channel 3, despite the pronounced modes of both distributions (Fig. 7c), the two distributions are not easily distinguishable and the two modes are very close. However, as shown in Fig. 7f, BTD (Ch4, Ch3) demonstrates fairly distinctive distributions with pronounced modes. It is tempting, therefore, to use the BTD (Ch3, Ch4) as input feature to SOFM, as opposed to using the combination of two channels. Theoretically, we can argue that using BTD reduces the dimensionality of the SOFM classification problem and that it would be consistent with the findings of several previously referenced studies in term of improving the R/NR delineation. However, in practice, with ETS = 0.255, the performance of BTD (Ch4, Ch3) is lower than the 0.295 ETS value associated with the combination of Ch3 and Ch4 as two independent input features. From Fig. 7 we can also infer that although channels 2, 4, and 6 (Figs. 7b,d,e, respectively) show some distinct differences between their relevant distributions, the absence of a pronounced mode for rainy condition for bands 4 and 6 may have contributed to their low performance in single-channel mode.

As seen in Table 1, of the 31 spectral combinations, only 7 are suitable for both day and nighttime rain area

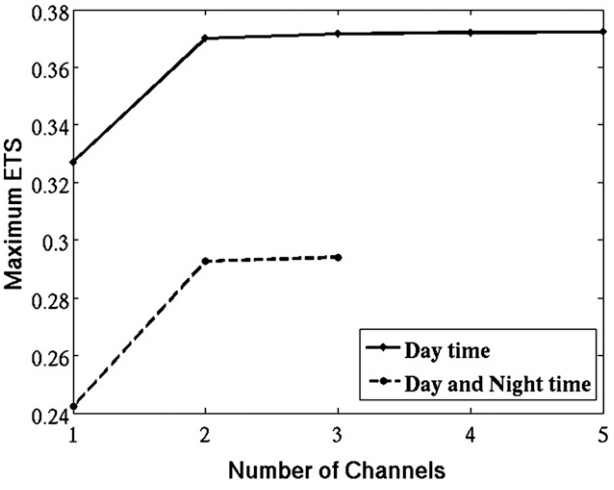

FIG. 8. Effect of the number of channels on the performance measure (ETS) using the best ranked combination within each category shown in Table 1.

detection. Although the values of the performance index for these combinations are below those of combinations that include visible albedo or Ch2, they provide an important niche in nighttime R/NR detection. Figure 8 shows the best performance (maximum ETS) within each set of 1–5-channel combinations plotted against the number of channels. Notice that for nighttime, a maximum of only three channels is available (3, 4, and 6). In both cases, ETS is stabilized using two channels. In other words, although using two channels shows considerable improvement over a single channel, only marginal improvement is achieved once more than two channels are used. However, this conclusion is only applicable to channels tested in this study and cannot be extended, without investigation, into other spectral bands.

6. Case studies

Two specific case studies are selected for assessing the relative usefulness of various channels and combinations of them at event scale. The first case, shown in Fig. 9, represents cold but thin nonraining clouds over Arkansas and Missouri, captured by a *GOES-12* image at 2015 UTC 9 June 2006. The second case study, shown in Fig. 10, was sampled at 1415 UTC 30 August 2006 from an extreme event (Hurricane Ernesto) as it passed over the Florida peninsula. Only 11 out of the 31 possible combinations are used in the analyses shown in Figs. 9, 10, with the majority representing thermal channels (3, 4, and 6) to assess both daytime and nighttime performances.

a. Nonraining cold, thin cloud

The Tb image (Fig. 9a) shows a relatively cold cloud over the region; the visible albedo image (Fig. 9b) presents a generally low reflectance, and the baseline R/NR data from radar (Fig. 9c) does not include any pixels with rain. The remaining panels (Figs. 9d–n) show R/NR maps produced by applying the trained networks of the corresponding combinations. The numbers on the top-right side of each panel represent false alarm counts. Figures 9d,e,f show the rain areas falsely detected by using single IR-only channels (3, 4, and 6). Clearly, all three channels failed to screen no-rain pixels, with Ch3 and Ch6 being close in terms of the number of false detections. Using Ch4, on the other hand, resulted in a slightly better performance. Consistent with the results reported so far, by combining two single channels (Figs. 9g,h,i), the SOFM displays a remarkable ability to extract information from each element of the combinations and substantially reduce false detection. The two dimensional (Ch3 + Ch4) combination also outperforms the single dimension BTD (Ch4, Ch3), suggesting that although subtracting the brightness temperatures appears to be useful, using the two channels as distinct input features increases the extraction efficiency of the SOFM. The relatively poor performance of the Ch3 + Ch6 combination also highlights the important role of Ch4 in R/NR detection, especially for nighttime. Only minor improvements can be gained by adding a third channel, as seen in Fig. 9k, for example, which is consistent with the validation results shown in Table 1. Remarkably, the introduction of albedo only (Fig. 9m) results in full removal of the no-rain pixels, even without the benefit of any IR information. Another interesting observation is the excellent performance of Ch2 (Fig. 9l) when compared with other single IR channels. In addition to the channel's sensitivity to cloud-top physical properties (Arking and Childs 1985; Rosenfeld and Gutman 1994), the presence of visible component is a likely cause of its improved performance.

b. Warm raining cloud (Hurricane Ernesto)

The panels in Fig. 10 are constructed in similar manner to Fig. 9. However, in this case, statistics (Table 2) from the contingency table were calculated for each scenario by counting the *H*'s, *M*'s, and *F*'s, which are shown in green, blue, and red, respectively. The Tb image (Fig. 10a) shows a relatively warm cloud area over the northwestern part of the Florida peninsula, with fairly high albedo (Fig. 10b) indicating thick clouds (zone A). Figure 10c shows the extent of the rain area as captured by radar. Clearly, the warmer cloud (zone A) is associated with rain. As seen in Figs. 10d,e,f, all three single IR channels (i) failed to capture the warm rain pixels particularly in zone A, (ii) successfully captured very cold rain pixels, and (iii) presented extensive false detections (red regions). Evidently, the high POD

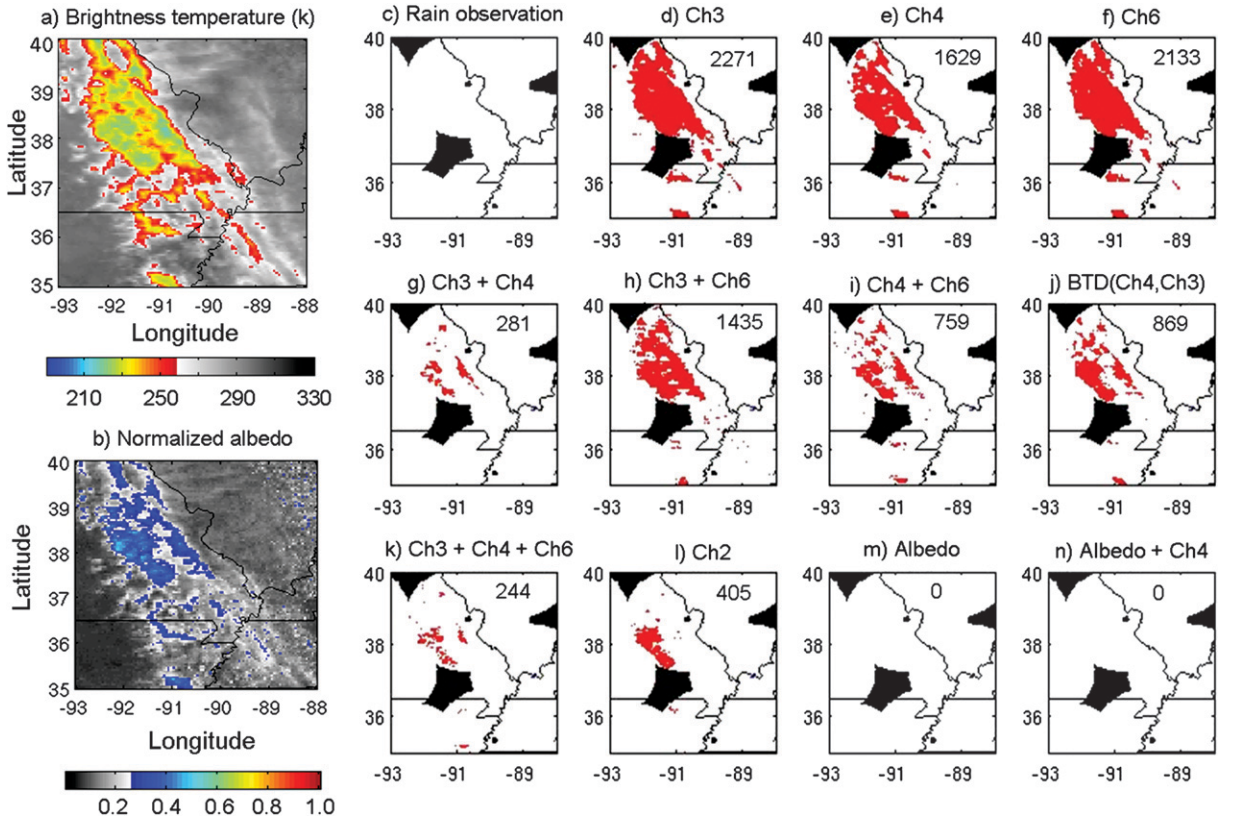

FIG. 9. Visual comparison of performances of selected channel combinations for a cold, thin cloud situation at 2015 UTC 9 Jun 2006: (a) map of Tb (Ch4), (b) map of normalized albedo, and (c) radar R/NR observation. (d)–(n) show the calculated R/NR areas using number of selected combinations. (top right) Number in each box represents the number of false alarm pixels indicated in red. Blacked-out blocks have no data.

associated with these three channels is not necessarily synonymous with good performance, as indicated by the high values of FAR as well as by the lower values of ETS.

Again, the introduction of one additional IR channel (Figs. 10g,h,i) significantly improves the algorithm's ability not only to screen cold no-rain areas but also to detect warm rain areas. This is particularly evident when the combination Ch4 + Ch3 is used (Fig. 10g). Consistently throughout this study, there seems to be no substantial advantage of using BTD (Ch4, Ch3) (Fig. 10j) as a single input feature over using the combination of Ch4 and Ch3 (Fig. 10g). Although reasonable improvements are observed using Ch2 (Fig. 10l), during daytime the improvements are very comparable to the gains made by using the combination of Ch3 and Ch4. Again, the most remarkable improvements in both detection and screening are achieved by using visible albedo alone, and the addition of an IR channel (Ch4) did not necessarily result in substantial gains. It must be mentioned that the above analysis may have been affected, to one degree or another, by errors due to temporal gaps between satellite images and ground observations, particularly considering the rapid movement of the hurricane.

7. Summary and conclusions

We presented an algorithm that allows the utilization of multiple channels in delineating R/NR areas. The algorithm was employed, as a framework, to equitably compare the value of information gained by using one or more spectral bands in detecting R/NR areas. Algorithm development and validation were conducted using a three-month period of coincident radar rainfall estimates and *GOES-12* images, and all possible 31 combinations of the 5 spectral bands were assessed. It must be mentioned that since the emitted radiance values for Ch2 (3.9 μm) of *GOES-12* are very low, there are issues with the reliability of radiance values for cold (below 230 K) clouds at night. However, the addition of reflected solar radiation during the daytime alleviates this problem. Therefore, Ch2 is useful after normalizing the reflection component for sun angle changes in manners similar to that used for Ch1 albedo correction, keeping in

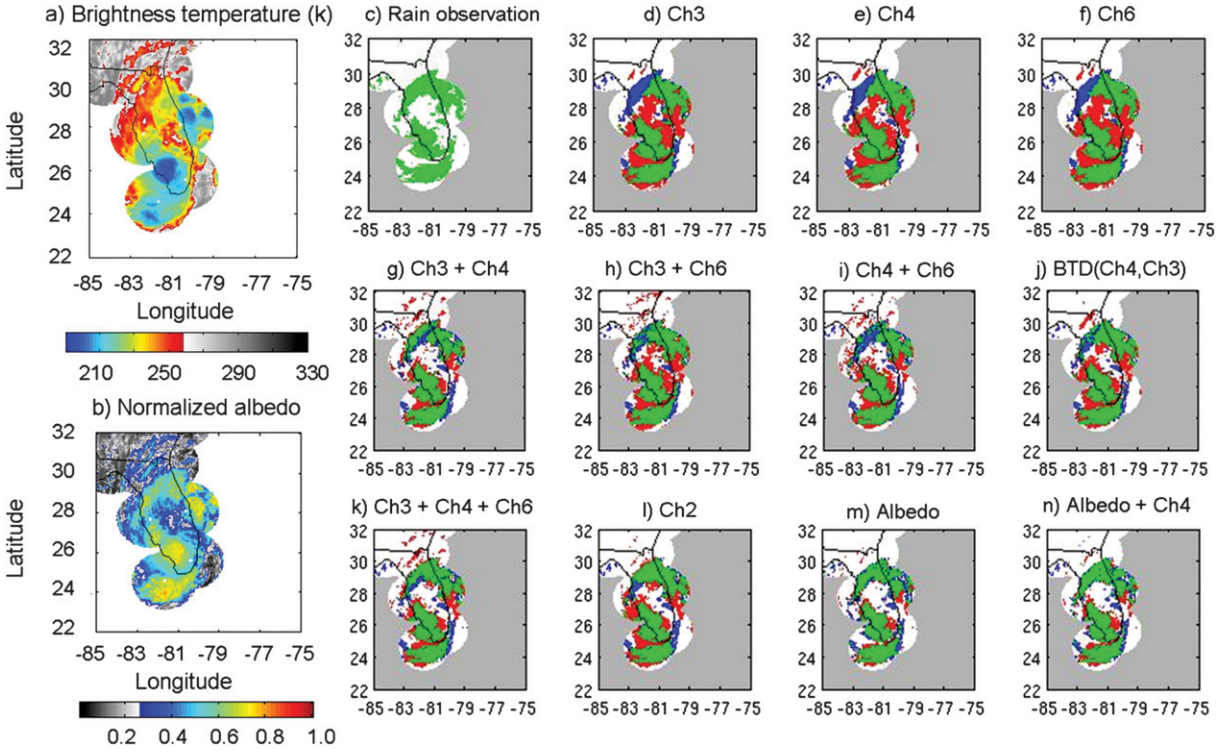

FIG. 10. Visual comparison of performances of the selected channel combinations for Hurricane Ernesto at 1415 UTC 30 Aug 2006: (a) Tb (Ch4), (b) normalized albedo, and (c) radar R/NR observation. (d)–(n) Calculated R/NR areas using number of selected combinations. Green, blue, and red indicate hits, misses, and false alarms, respectively.

mind that just as with visible albedo, all scenarios containing Ch2 are only applicable to the daytime period.

Our results demonstrate that during the daytime, significant improvement in R/NR detection can be gained by using albedo alone. We found that albedo improves both the detection of rain pixels and the screening of no-rain pixels. Additional improvements were also obtained by using albedo in conjunction with other channels. However, only marginal improvement is gained when it is combined with more than one IR/NIR channel.

For nighttime detection, when visible channels are not available, the results demonstrated that significant improvement in increasing the hits and decreasing the false alarms and misses can be achieved by using the water vapor channel (Ch3; 6.5 μm) together with the thermal channel (Ch4; 10.7 μm), compared to using Ch4 alone. Because of the availability of these two channels on almost all environmental weather satellites, this combination has the potential to be applied for current satellites. Although using combinations of any two IR channels seems superior to use of any single IR channel, no significant improvement is found when more than two infrared channels are used.

Our results demonstrate the capability of SOFM to identify the most important channels for rain detection and to extract the information required for improved detection of rain pixels and screening of no-rain pixels. Furthermore, the extensibility of the proposed algorithm to use any number of spectral bands that are available from other imagers lends its particular strength in cases in which the physical relationship between the spectral band and rainfall process is not clear.

With the advent of modern imagers on recent and future geostationary satellites [e.g., SEVERI on MSG and the

TABLE 2. Statistics for selected scenarios for Hurricane Ernesto at 1415 UTC 30 Aug 2006

Scenario	POD (%)	FAR (%)	BIAS	ETS	ETS gain over Ch4 alone (%)
Ch3	73.844	44.461	1.330	0.254	−12.41
Ch6	78.216	44.052	1.398	0.272	−6.32
Ch4	76.843	41.997	1.325	0.290	0
Ch3 + Ch4	77.573	34.122	1.178	0.377	29.93
Ch3 + Ch6	80.408	41.834	1.382	0.304	4.81
Ch4 + Ch6	72.231	38.978	1.184	0.305	4.92
BTD (Ch4, Ch3)	79.728	37.415	1.274	0.352	21.09
Ch3 + Ch4 + Ch6	78.125	34.655	1.196	0.373	28.48
Ch2	80.635	35.704	1.254	0.375	28.99
Albedo	75.117	22.319	0.967	0.478	64.63
Albedo + Ch4	79.224	24.159	1.045	0.489	68.44

Advanced Baseline Imager (ABI) on GOES-R], more spectral channels with higher temporal and spatial resolution are becoming available. This study, along with some previous works, confirms the inherent benefit of additional spectral bands for precipitation retrievals. As mentioned by Huffman et al. (2007), enhancing GEO-based rain retrieval algorithms is an important step toward improving combined LEO (PMW) and GEO-based precipitation products. Together with the anticipated launch of NASA's Global Precipitation Measurement (GPM) mission, multispectral approaches that use data from recent and future GEO satellites provide an unprecedented opportunity to improve global precipitation measurements at scales relevant to many applications.

Acknowledgments. Partial financial support is made available from NASA Earth and Space Science Fellowship (NESSF award NNX08AU78H), NASA-PMM (Grant NNG04GC74G), NOAA/NESDIS GOES-R Program Office (GPO) via the GOES-R Algorithm Working Group (AWG), NSF STC for Sustainability of Semi-Arid Hydrology and Riparian Areas (SAHRA; Grant EAR-9876800), and NASA NEWS (Grant NNX06AF934) programs. The authors thank Mr. Dan Braithwaite for his technical assistance on processing the satellite/radar data for this experiment. The contents of this paper are solely the opinion of the authors and do not constitute a statement of policy, decision, or position on behalf of the GOES-R Program Office, NOAA, or the U. S. government.

REFERENCES

Ackerman, S. A., 1996: Global satellite observations of negative brightness temperature differences between 11 and 6.7 μm. *J. Atmos. Sci.,* **53,** 2803–2812.

Adler, R. F., and A. J. Negri, 1988: A satellite infrared technique to estimate tropical convective and stratiform rainfall. *J. Appl. Meteor.,* **27,** 30–51.

——, ——, P. R. Keehn, and I. M. Hakkarinen, 1993: Estimation of monthly rainfall over Japan and surrounding waters from a combination of low-orbit microwave and geosynchronous IR data. *J. Appl. Meteor.,* **32,** 335–356.

Arkin, P. A., and P. Xie, 1994: The Global Precipitation Climatology Project: First algorithm intercomparison project. *Bull. Amer. Meteor. Soc.,* **75,** 401–419.

Arking, A., and J. D. Childs, 1985: Retrieval of cloud cover parameters from multispectral satellite images. *J. Climate Appl. Meteor.,* **24,** 322–333.

Ba, M. B., and A. Gruber, 2001: GOES multispectral rainfall algorithm (GMSRA). *J. Appl. Meteor.,* **40,** 1500–1514.

Capacci, D., and B. J. Conway, 2005: Delineation of precipitation areas from MODIS visible and infrared imagery with artificial neural networks. *Meteor. Appl.,* **12,** 291–305.

Cheng, M., and R. Brown, 1995: Delineation of precipitation areas by correlation of Meteosat visible and infrared data with radar data. *Mon. Wea. Rev.,* **123,** 2743–2757.

——, ——, and C. C. Collier, 1993: Delineation of precipitation areas using Meteosat infrared and visible data in the region of the United Kingdom. *J. Appl. Meteor.,* **32,** 884–898.

Gilbert, G. F., 1884: Finley's tornado predictions. *Amer. Meteor. J.,* **1,** 166–172.

Grassotti, C., and L. Garand, 1994: Classification-based rainfall estimation using satellite data and numerical forecast model fields. *J. Appl. Meteor.,* **33,** 159–178.

Griffith, C. G., W. L. Woodley, P. G. Grube, D. W. Martin, J. Stout, and D. N. Sikdar, 1978: Rain estimation from geosynchronous satellite imagery—Visible and infrared studies. *Mon. Wea. Rev.,* **106,** 1153–1171.

Hsu, K.-L., X. Gao, S. Sorooshian, and H. V. Gupta, 1997: Precipitation estimation from remotely sensed information using artificial neural networks. *J. Appl. Meteor.,* **36,** 1176–1190.

——, H. V. Gupta, X. Gao, and S. Sorooshian, 1999: Estimation of physical variables from multichannel remotely sensed imagery using a neural network: Application to rainfall estimation. *Water Resour. Res.,* **35,** 1605–1618.

Huffman, G. J., R. F. Adler, M. M. Morrissey, D. T. Bolvin, S. Curtis, R. Joyce, B. McGavock, and J. Susskind, 2001: Global precipitation at one-degree daily resolution from multisatellite observations. *J. Hydrometeor.,* **2,** 36–50.

——, and Coauthors, 2007: The TRMM Multisatellite Precipitation Analysis (TMPA): Quasi-global, multiyear, combined-sensor precipitation estimates at fine scales. *J. Hydrometeor.,* **8,** 38–55.

Inoue, T., 1987: A cloud type classification with NOAA 7 split-window measurements. *J. Geophys. Res.,* **92,** 3991–4000.

——, and K. Aonashi, 2000: A comparison of cloud and rainfall information from instantaneous visible and infrared scanner and precipitation radar observations over a frontal zone in East Asia during June 1998. *J. Appl. Meteor.,* **39,** 2292–2301.

Jolliffe, I. T., and D. B. Stephenson, 2003: *Forecast Verification: A Practitioner's Guide in Atmospheric Science*. John Wiley & Sons, 240 pp.

Joyce, R. J., J. E. Janowiak, P. A. Arkin, and P. Xie, 2004: CMORPH: A method that produces global precipitation estimates from passive microwave and infrared data at high spatial and temporal resolution. *J. Hydrometeor.,* **5,** 487–503.

Kidd, C., D. R. Kniveton, M. C. Todd, and T. J. Bellerby, 2003: Satellite rainfall estimation using combined passive microwave and infrared algorithms. *J. Hydrometeor.,* **4,** 1088–1104.

King, P. W. S., W. D. Hogg, and P. A. Arkin, 1995: The role of visible data in improving satellite rain-rate estimates. *J. Appl. Meteor.,* **34,** 1608–1621.

Kohonen, T., 1982: Self-organized formation of topologically correct feature maps. *Biol. Cybern.,* **43,** 59–69.

Kuligowski, R. J., 2002: A self-calibrating real-time GOES rainfall algorithm for short-term rainfall estimates. *J. Hydrometeor.,* **3,** 112–130.

Kummerow, C., and L. Giglio, 1995: A method for combining passive microwave and infrared rainfall observations. *J. Atmos. Oceanic Technol.,* **12,** 33–45.

——, W. S. Olson, and L. Giglio, 1996: A simplified scheme for obtaining precipitation and vertical hydrometeor profiles from passive microwave sensors. *IEEE Trans. Geosci. Remote Sens.,* **34,** 1213–1232.

Kurino, T., 1997: A satellite infrared technique for estimating ''deep/shallow'' precipitation. *Adv. Space. Res.,* **19,** 511–514.

Lensky, I. M., and D. Rosenfeld, 2003: A night-rain delineation algorithm for infrared satellite data based on microphysical considerations. *J. Appl. Meteor.,* **42,** 1218–1226.

Levizzani, V., F. Porcú, F. S. Marzano, A. Mugnai, E. A. Smith, and F. Prodi, 1996: Investigating a SSM/I microwave algorithm to calibrate METEOSAT infrared instaneous rainrate estimates. *Meteor. Appl.,* **3,** 5–17.

Lin, Y., and K. E. Mitchell, 2005: The NCEP stage II/IV hourly precipitation analyses: Development and applications. Preprints, *19th Conf. on Hydrology,* San Diego, CA, Amer. Meteor. Soc., 1.2. [Available online at http://ams.confex.com/ams/pdfpapers/83847.pdf.]

Lovejoy, S., and G. L. Austin, 1979: The delineation of rain areas from visible and IR satellite data for GATE and mid-latitudes. *Atmos.–Ocean,* **17,** 77–92.

Maddox, R. A., J. Zhang, J. J. Gourley, and K. W. Howard, 2002: Weather radar coverage over the contiguous United States. *Wea. Forecasting,* **17,** 927–934.

Martin, D. W., R. A. Kohrs, F. R. Mosher, C. M. Medaglia, and C. Adamo, 2008: Over-ocean validation of the global convective diagnostic. *J. Appl. Meteor. Climatol.,* **47,** 525–543.

Miller, S. W., P. A. Arkin, and R. Joyce, 2001: A combined microwave/infrared rain rate algorithm. *Int. J. Remote Sens.,* **22,** 3285–3307.

Minnis, P., and E. F. Harrison, 1984: Diurnal variability of regional cloud and clear-sky radiative parameters derived from GOES data. 1. Analysis method. *J. Climate Appl. Meteor.,* **23,** 993–1011.

Nakajima, T., and M. D. King, 1990: Determination of the optical thickness and effective particle radius of clouds from reflected solar radiation measurements. Part I: Theory. *J. Atmos. Sci.,* **47,** 1878–1893.

——, ——, J. D. Spinhirne, and L. F. Radke, 1991: Determination of the optical thickness and effective particle radius of clouds from reflected solar radiation measurements. Part II: Marine stratocumulus observations. *J. Atmos. Sci.,* **48,** 728–751.

Negri, A. J., and R. F. Adler, 1987a: Infrared and visible satellite rain estimation. Part I: A grid cell approach. *J. Climate Appl. Meteor.,* **26,** 1553–1564.

——, and ——, 1987b: Infrared and visible satellite rain estimation. Part II: A cloud definition approach. *J. Climate Appl. Meteor.,* **26,** 1565–1576.

O'Sullivan, F., C. H. Wash, M. Stewart, and C. E. Motell, 1990: Rain estimation from infrared and visible GOES satellite data. *J. Appl. Meteor.,* **29,** 209–223.

Pilewskie, P., and S. Twomey, 1987: Cloud phase discrimination by reflectance measurements near 1.6 and 2.2 μm. *J. Atmos. Sci.,* **44,** 3419–3420.

Rosenfeld, D., and G. Gutman, 1994: Retrieving microphysical properties near the tops of potential rain clouds by multispectral analysis of AVHRR data. *Atmos. Res.,* **34,** 259–283.

——, and I. M. Lensky, 1998: Satellite–based insights into precipitation formation processes in continental and maritime convective clouds. *Bull. Amer. Meteor. Soc.,* **79,** 2457–2476.

Schaefer, J. T., 1990: The critical success index as an indicator of warning skill. *Wea. Forecasting,* **5,** 570–575.

Schmetz, J., S. A. Tjemkes, M. Gube, and L. Van de berg, 1997: Monitoring deep convection and convective overshooting with METEOSAT. *Adv. Space Res.,* **19,** 433–441.

Sorooshian, S., K.-L. Hsu, X. Gao, H. V. Gupta, B. Imam, and D. Braithwaite, 2000: Evaluation of PERSIANN system satellite–based estimates of tropical rainfall. *Bull. Amer. Meteor. Soc.,* **81,** 2035–2046.

Tapiador, F. J., C. Kidd, K.-L. Hsu, and F. Marzano, 2004: Neural networks in satellite rainfall estimation. *Meteor. Appl.,* **11,** 83–91.

Tian, Y., C. D. Peters-Lidard, B. J. Choudhury, and M. Garcia, 2007: Multitemporal analysis of TRMM-based satellite precipitation products for land data assimilation applications. *J. Hydrometeor.,* **8,** 1165–1183.

Tjemkes, S., L. van de Berg, and J. Schmetz, 1997: Warm water vapor pixels over high clouds as observed by METEOSAT. *Beitr. Phys. Atmos.,* **70,** 15–21.

Todd, M. C., C. Kidd, D. Kniveton, and T. J. Bellerby, 2001: A combined satellite infrared and passive microwave technique for estimation of small-scale rainfall. *J. Atmos. Oceanic Technol.,* **18,** 742–755.

Tsonis, A. A., 1984: On the separability of various classes from the GOES visible and infrared data. *J. Appl. Meteor.,* **23,** 1393–1410.

——, 1988: Single thresholding and rain area delineation from satellite imagery. *J. Appl. Meteor.,* **27,** 1302–1306.

——, and G. A. Isaac, 1985: On a new approach for instantaneous rain area delineation in the midlatitudes using GOES data. *J. Climate Appl. Meteor.,* **24,** 1208–1218.

Turk, F. J., J. Hawkins, E. A. Smith, F. S. Marzano, A. Mugnai, and V. Levizzani, 2000: Combining SSM/I, TRMM and infrared geostationary satellite data in a near-realtime fashion for rapid precipitation updates: Advantages and limitations. *Proc. EUMETSAT Meteorological Satellite Data Users' Conf.,* Vol. 2, Bologna, Italy, EUMETSAT, 705–707.

——, E. E. Ebert, H.-J. Oh, B.-J. Sohn, V. Levizzani, E. A. Smith, and R. R. Ferraro, 2003: Validation of an operational global precipitation analysis at short time scales. Preprints, *12th Conf. on Satellite Meteorology and Oceanography,* Long Beach, CA, Amer. Meteor. Soc., JP1.2. [Available online at http://ams.confex.com/ams/pdfpapers/56865.pdf.]

Vicente, G. A., R. A. Scofield, and W. P. Menzel, 1998: The operational GOES infrared rainfall estimation technique. *Bull. Amer. Meteor. Soc.,* **79,** 1883–1898.

Weng, F. Z., L. M. Zhao, R. R. Ferraro, G. Poe, X. F. Li, and N. C. Grody, 2003: Advanced microwave sounding unit cloud and precipitation algorithms. *Radio Sci.,* **38,** 8068, doi:10.1029/2002RS002679.

Wu, R., J. A. Weinman, and R. T. Chin, 1985: Determination of rainfall rates from GOES satellite images by a pattern recognition technique. *J. Atmos. Oceanic Technol.,* **2,** 314–330.

Xu, L., X. Gao, S. Sorooshian, P. A. Arkin, and B. Imam, 1999: A microwave infrared threshold technique to improve the GOES precipitation Index. *J. Appl. Meteor.,* **38,** 569–579.

Zhao, L. M., and F. Z. Weng, 2002: Retrieval of ice cloud parameters using the advanced microwave sounding unit. *J. Appl. Meteor.,* **41,** 384–395.